Static and dynamic magnetic properties of $Ni_{80}Fe_{20}$ anti-ring nanostructures

J. Ding,[1] N. Singh,[2] M. Kostylev,[3] and A. O. Adeyeye[1,*]

[1]*Information Storage Materials Laboratory, Department of Electrical and Computer Engineering, National University of Singapore, Singapore 117576*

[2]*A*Star, Institute of Microeletronics, 11 Science Park Road, Singapore Science Park II, Singapore 117685*

[3]*School of Physics, University of Western Australia, Crawley, Western Australia 6009, Australia*

(Received 10 December 2012; revised manuscript received 18 April 2013; published 8 July 2013)

The static and dynamic behavior of $Ni_{80}Fe_{20}$ anti-ring arrays has been systematically investigated using broadband ferromagnetic resonance (FMR) spectroscopy, magneto-optical Kerr effect (MOKE), and magnetic force microscopy (MFM). The unit cell of this periodic lattice represents a hole in a continuous film, with an elliptical nanodot placed in the middle of the hole. The FMR responses display multiple absorption peaks due to the superposition of the absorptions from the anti-dot and the central nanomagnet (dot) regions of the anti-ring structures. Interestingly, for fixed anti-ring geometry, the static and dynamic behavior is markedly sensitive to the thickness of the structure due to complicated spatial distributions of the demagnetizing field. Direct MFM imaging reveals that at remanence, the central nanomagnets are in a single-domain state, for small sample thicknesses, whereas for larger thicknesses, they display a multidomain or vortex state. This observation is in good agreement with both FMR and MOKE data. All our results agree well with micromagnetic simulations.

DOI: 10.1103/PhysRevB.88.014301 PACS number(s): 75.40.Cx, 75.40.Gb, 76.50.+g, 75.75.−c

I. INTRODUCTION

Advancements in lithography tools for fabricating nanostructures with precisely controlled dimensions and geometry offer a unique opportunity to design and prepare a variety of nanopatterned ferromagnetic films.[1] It is predictable that the periodically patterned magnetic media at the nanoscale will be used in the future.[2] Minibands consisting of allowed spin-wave (SW) frequencies and forbidden frequency gaps have been observed in the so-called magnonic crystals (MCs).[2–4] MC, conceived as the magnetic analog of photonic crystal (PC), has attracted much interest both from a fundamental viewpoint and because of their potential applications in microwave devices[5] and magnetic logic devices.[6]

SW propagation in MCs is much more complex than that of photons in PC, since it depends on the relative orientation between the magnetization and the wave vector.[2] There are various factors that influence the magnetization state of the MCs, such as the history of the applied magnetic field,[7,8] the anisotropy of the materials, and the structural variations.[9,10] Patterning continuous films produces demagnetizing fields that modify the magnetic ground state and the dynamic dipole energy. This effect becomes more important when the patterns shrink to the nanoscale.[2] A number of nanoscale patterns have been introduced to design MCs such as shallow grooves etched in films,[11] synthetic nanostructures composed of alternating $Ni_{80}Fe_{20}$ nanowires (NWs) in direct contact with Co NWs,[12] and homogeneous NWs separated by a nanoscale air gap.[13]

Magnetic anti-dots, which are periodic arrays of holes, patterned into a thin film represent a two dimensional (2D) MC[2,10] in which the magnonic band structures can be engineered by varying the periodicity of the arrays. The static and dynamic properties of magnetic anti-dot nanostructures have been extensively investigated.[14–18] Recently, we have demonstrated experimentally that a bicomponent $Ni_{80}Fe_{20}$ anti-dot array, consisting of holes with alternating diameters, provides more controllable static and dynamic properties.[19] Another proposed design to further manipulate SW properties in 2D structure is the bicomponent anti-dot lattice with embedded Co nanodisks.[20] The Fe-filled $Ni_{80}Fe_{20}$ anti-dot nanostructure has also been discussed as they provide more degrees of freedom to control the static and dynamic behavior in the structure.[21]

In this paper, we report on a systematic investigation of the static and dynamic response in $Ni_{80}Fe_{20}$ anti-ring arrays using broadband ferromagnetic resonance (FMR) spectroscopy, magneto-optical Kerr effect (MOKE), and magnetic force microscopy (MFM). The anti-rings represent a natural extension of the anti-dot geometry, in which each of the holes (anti-dots) hosts a nanodot (central nanomagnet), which is separated from the anti-dot lattice by a nonmagnetic gap. The FMR response of the anti-rings is highly sensitive to the nanostructure magnetization state for a fixed film thickness. The dynamic behavior of the surrounding rectangular anti-dot can be modified by controlling the magnetization state of the central elliptical nanomagnet. We have also found that both static and dynamic responses of the structure are adjustable by changing the film thickness. The MOKE and MFM results show that the central nanomagnets remain in the saturated state for smaller sample thicknesses, while a multidomain state or vortex state can be observed for thicker nanostructures.

We validated our experimental results with micromagnetic simulations of microwave magnetization dynamics. The micromagnetic simulations show that the resonance frequency of the anti-dot can be used to detect the magnetic properties of the central nanomagnets. This may help to design new bioanalytical measurement tools for lab-on-a-chip applications in future.[22]

This paper is organized as follows. In Sec. II, we give the details of the samples, the method of the fabrication, and the characterization procedures. In Sec. III. we present and discuss the results obtained on a 30-nm-thick anti-ring array. In Sec. IV, we discuss the effect of the sample thickness on the magnetic properties of the anti-rings. Secs. IV A and B focus on the static and dynamic responses of the structure,

respectively. We present detailed results of the micromagnetic modeling in Sec. IV C. The goal of this section is to check whether the dynamic behaviors of anti-dot nanostructures can be used to detect the magnetic properties of the central nanomagnets.

II. DETAILS OF THE EXPERIMENT

The large area (4×4 mm^2) anti-ring structures were fabricated on a commercially available silicon substrate using deep ultraviolet lithography at 248-nm exposure wavelength followed by e-beam evaporation of $Ni_{80}Fe_{20}$ films and ultrasonic-assisted liftoff in OK73 resist thinner. The film thickness (t) is varied in a range from 8 to 40 nm. Details of the fabrication process are described in Ref. 23. A scanning electron microscope (SEM) was used to check for liftoff completion and to determine the actual sizes of the nanostructure. A representative SEM image of an anti-ring array is shown in Fig. 1(a). Figure 1(b) shows a schematic diagram of the sample structure and the field configuration. The x, y, and z (out-of-plane) axes of a Cartesian frame of reference are parallel to the major axis (850 nm), minor axis (550 nm) of the outer anti-ring edge, and to the thickness of the anti-ring structure, respectively. An elliptical 455-nm-long and 280-nm-wide nanomagnet is placed at the center of each unit to complete the anti-ring geometry. The edge-to-edge spacing of the adjacent anti-ring cells is kept at 200 nm along the x and y directions.

The FMR responses were measured in the 1- to 20-GHz frequency range using a broadband microwave vector network analyzer. To obtain the high-frequency response, the sample was positioned on top of a microstrip board, with the nanostructure facing the board, similar to the technique reported in Ref. 24. The external static magnetic field (H_{app}) is applied along the x axis, whereas the microwave magnetic field h_f produced by the microstrip is perpendicular to H_{app} (along the y axis). The microwave transmission line measurements were performed at room temperature by sweeping the frequency in the 1- to 20-GHz range for a fixed H_{app}. This was repeated for different H_{app} values starting from the negative saturation field $-H_{sat}$, passing through zero, and then gradually increasing it to H_{sat}. The field is then subsequently decreased to $-H_{sat}$.

The static magnetic properties of the anti-ring arrays were measured using a MOKE system with a spot size of about 50 μm. The magnetic spin configurations of the nanostructure

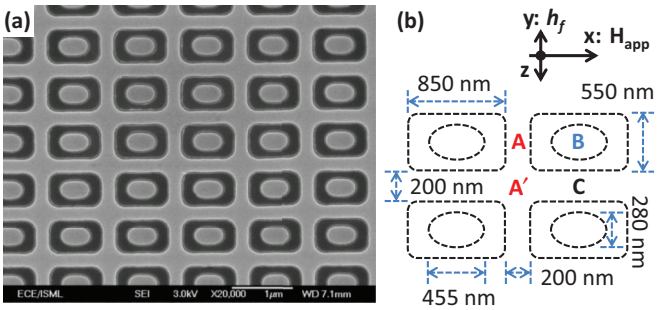

FIG. 1. (Color online) (a) Scanning electron micrographs image of 30-nm-thick $Ni_{80}Fe_{20}$ anti-ring arrays. (b) Structure of the sample and field configuration of the measurement.

were imaged using the MFM imaging in the phase detection mode with commercial CoCr-coated Si cantilever tips magnetized along the tip axis. The scan height was maintained at a constant distance of 40 nm.

Interpretation of the field dispersion of FMR modes was obtained using the LLG Micromagnetic Simulator.[25] The simulation was carried out using the SEM image as a bitmap with periodic boundary conditions. The standard parameters for $Ni_{80}Fe_{20}$ (gyromagnetic ratio $\gamma = 2.8$ GHz/kOe, saturation magnetization $M_s = 800$ kAm^{-1}, exchange constant $A = 13 \times 10^{-12}$ Jm^{-1}, damping constant $= 0.008$ and anisotropy constant $K_U = 0$) were used in the simulation. We have quantified the spatial characteristics of different modes using time-dependent micromagnetic simulations and analyzed the results using spatially and frequency-resolved fast Fourier transform (FFT) imaging.[26–28]

III. 30-NM-THICK ANTI-RING ARRAY

In this section, we show both experimental and simulated results for one of the anti-ring arrays. We concentrate on the 30-nm-thick nanostructure to discuss the static and dynamic behavior of the anti-ring array for different magnetization states. The analysis is also correlated to the previous results for anti-dots and nanomagnets. The main goal of this section is to verify that the dynamic responses of the anti-ring structure are markedly sensitive to the magnetization state of the central nanomagnet.

The normalized magnetic hysteresis loops were characterized using the MOKE setup with the field applied along the x axis of the nanostructure as shown in Fig. 2(a). For clarity, the following discussion is based on only one half of the loop, from the negative to the positive saturation. The anti-ring array is saturated with $H_{app} = -1500$ Oe. A multistep switching process is observed in the transition field range (from -300 to 500 Oe). The switching starts with a gradual change in magnetization when H_{app} is in a field range from -300 to 40 Oe. This is attributed to the coherent rotation process for area A [inset in Fig. 2(a)], which is similar to the hard-axis switching process of single-domain magnets. A faster magnetization change is observed when H_{app} is increased from 40 to 180 Oe. The nucleation of the vortex core inside the central nanomagnet might be the main contributor to this increase. The switching of the main area of the nanostructure may be the main cause of the sharp increase in the magnetization for H_{app} in the range of 180 to 240 Oe. The annihilation of the vortex in the central nanomagnet and the magnetization rotation process for area A are the origins of the last part of the switching process of the nanostructure (between 240 and 500 Oe). The magnetic saturation is reached for the fields above 500 Oe.

We have also confirmed this switching scenario by micromagnetic simulations. The simulated hysteresis loop is shown in Fig. 2(b). There is a good agreement between the experimental results and the micromagnetic simulations. The magnetization states corresponding to various positions in the hysteresis loop are shown in the insets to Figs. 2(b) and 2(c). The switching fields are slightly different in the simulated hysteresis loop. For example, the position II (V) is for $H_{app} = -240$ Oe (240 Oe) in the experiment, while the simulation shows the similar switching process for

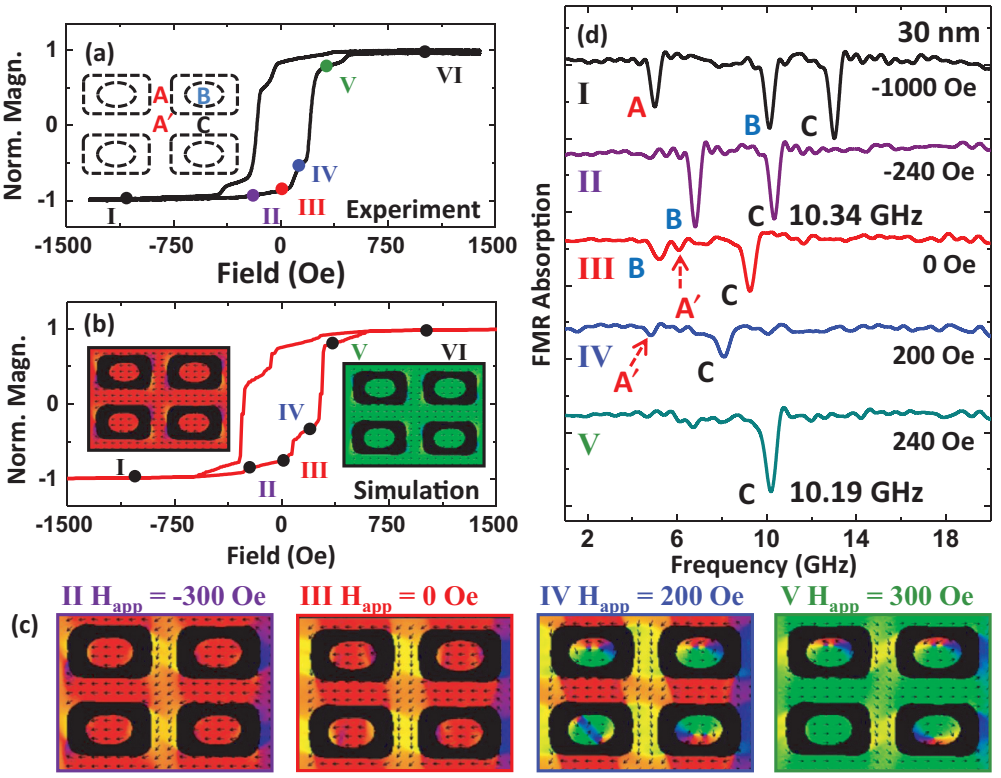

FIG. 2. (Color online) The measured (a) and simulated (b) M-H loops for 30-nm-thick $Ni_{80}Fe_{20}$ anti-ring array. Note the difference in H_{app} for the simulated and experimental magnetization states. The saturated magnetization state for $H_{app} = -1000$ and 1000 Oe are shown as the left and right insets of (b), respectively. The simulated magnetization states for $H_{app} = -300$, 0, 200, and 300 Oe are shown in (c). (d) Measured FMR absorption traces of the anti-ring array with varying H_{app}.

$H_{app} = -300$ Oe (300 Oe). The magnetization states shown in the insets to Fig. 2(b) suggest that the whole structure is almost saturated along the $-x$ axis and $+x$ axis for positions I and VI, respectively. The magnetization states II and III shown in Fig. 2(c) confirm that the gradual variation of magnetization in the field range from -300 to 40 Oe is attributed to the magnetization rotation process for area A. A multidomain state or vortex state can be observed for the central nanomagnets for position IV in the hysteresis loop. This confirms our analysis about the faster magnetization change in the field range from 40 to 180 Oe. After the sharp increase in magnetization around 220 Oe, the magnetization vector for the main area of the nanostructure is switched to along the x axis as shown in the magnetization state for position V. Some of the central nanomagnets are still in the vortex state, and the annihilation of the vortex cores represents the cause of the slow increase in magnetization in the field range from 240 to 500 Oe.

FMR measurements have been performed to further understand the magnetic properties of the anti-ring array. Shown in Fig. 2(d) are the representative FMR absorption curves as a function of the applied field H_{app}. In the saturated state ($H_{app} = -1000$ Oe), we observed three clear resonance modes (labeled as A, B, and C). It is easy to understand that the three modes originate from the resonances localized in spatial areas with different values of the internal magnetic field. The frequency position of the lowest-frequency mode A is consistent with the mode localized in area A of the anti-dot lattice. The two higher frequency modes B and C should then originate from areas B and C, respectively. The resonance frequency of mode C is higher than that of mode B due to the larger aspect ratio for area C. (We define the aspect ratio as the ratio of the area size along the field to its size in the perpendicular in-plane direction.) Peaks B and C shift to lower frequencies when H_{app} is increased to 0 Oe due to the reduction in the internal field, in agreement with the classical Kittel theory.[29] Meanwhile, mode A from trace I vanishes for $H_{app} = -240$ Oe (trace II), while a new mode (labeled as A′) emerges for $H_{app} = 0$ Oe (trace III). The disappearance of peak A is due to the fact that for smaller $|H_{app}|$ values the spins in area A rotate to along the edge of that area that is perpendicular to the H_{app} direction. The microwave magnetic field is now parallel to the direction of spins, which makes excitation of this mode inefficient. As a result, this mode is not seen in the absorption spectrum. The emerging mode A′ may be localized on the junction area (A′) of areas A and C. The spins in this area tend to align at 45° with the x axis as shown in the simulated magnetization state for positions III and IV in Fig. 2(c). We observed that the frequency and intensity of mode A′ are much lower than those of mode C, although they are in the same row of the nanostructure. The main cause of this phenomenon might be the decrease of the effective magnetization value along the H_{app} direction (x axis) due to the tilt of the magnetization in area A′. We have also noticed that the intensity of mode B is also reduced for $H_{app} = 0$ Oe. This may be due to the rotation of the spins in area B. Another possible reason for this decrease in intensity is the fact that

some of the central nanomagnets may form a vortex state for $H_{app} = 0$ Oe because of the significant thickness of the nanostructure.

For symmetry reasons, the radial modes of vortex resonance couple very inefficiently to the uniform in-plane microwave magnetic field. Therefore, there will be no noticeable resonance absorption for the nanomagnets with the vortex magnetization state.[30] This analysis is confirmed by the disappearance of mode B when the H_{app} is further increased to 200 Oe as the FMR absorption curve IV in Fig. 2(d) shows. The corresponding simulated magnetization state shown in Fig. 2(c), IV suggests that all the nanomagnets form a vortex or multidomain magnetization state. We also found that intensity of mode C reduces for this field. A possible cause for this phenomenon is that some more spins in area C have been switched or tilted when the reversal field is increased as shown in the simulated magnetization state [Fig. 2(c), IV]. A sharp frequency jump for mode C can be observed when H_{app} is increased from 200 to 240 Oe. This is due to the switching of most of the area of the nanostructure as the simulated magnetization state demonstrates [Fig. 2(c), V]. In this situation, the direction of the spins in area C is parallel to H_{app}, and the field value is 240 Oe. The direction of spins in area C relative to H_{app} is similar to that when $H_{app} = -240$ Oe [Fig. 2(c), II]. Interestingly, the resonance frequency of mode C for $H_{app} = 240$ Oe is 10.19 GHz, which is 0.15 GHz lower than that for $H_{app} = -240$ Oe. By comparing the simulated magnetization state V to II, we found that the only difference between these two states is the state of the central nanomagnets. This suggests coupling of these two areas by static and dynamic demagnetizing fields. The competition of these two types of coupling may be the main contributor to this phenomenon. This difference implies that the increase in the frequency of mode C for $H_{app} = -240$ Oe is possibly due to the dynamic coupling, i.e., due to repulsion of modes B and C for the single-domain state of the central dot (state II) and the absence of this repulsion for the vortex state (state V). In the former case, the repulsion should be quite strong in order to overcompensate the above-mentioned decrease in the frequency of mode C due to the static demagnetization. These results suggest that the dynamic behavior of the surrounding rectangular anti-dot can be modified by controlling the magnetization state of the central elliptical nanomagnet.

We further investigate the dynamic response of the nanostructure by measuring the absorption spectra for the forward half of the major hysteresis loop with H_{app} varying from -1500 to $+1500$ Oe [Fig. 3(a)]. This figure clearly shows the mode evolution trend for the nanostructure.

Dynamic micromagnetic simulation was carried out for a H_{app} range similar to the experimental one. Shown in Fig. 3(b) is the simulated FMR absorption curve for $H_{app} = -1000$, -300, 0, and 300 Oe. The simulated results reproduce most of the features of the experimentally observed FMR curves. Shown in Fig. 3(d) are simulated mode profiles. The FFT images are for the frequencies 6.02, 10.4, and 13.1 GHz,

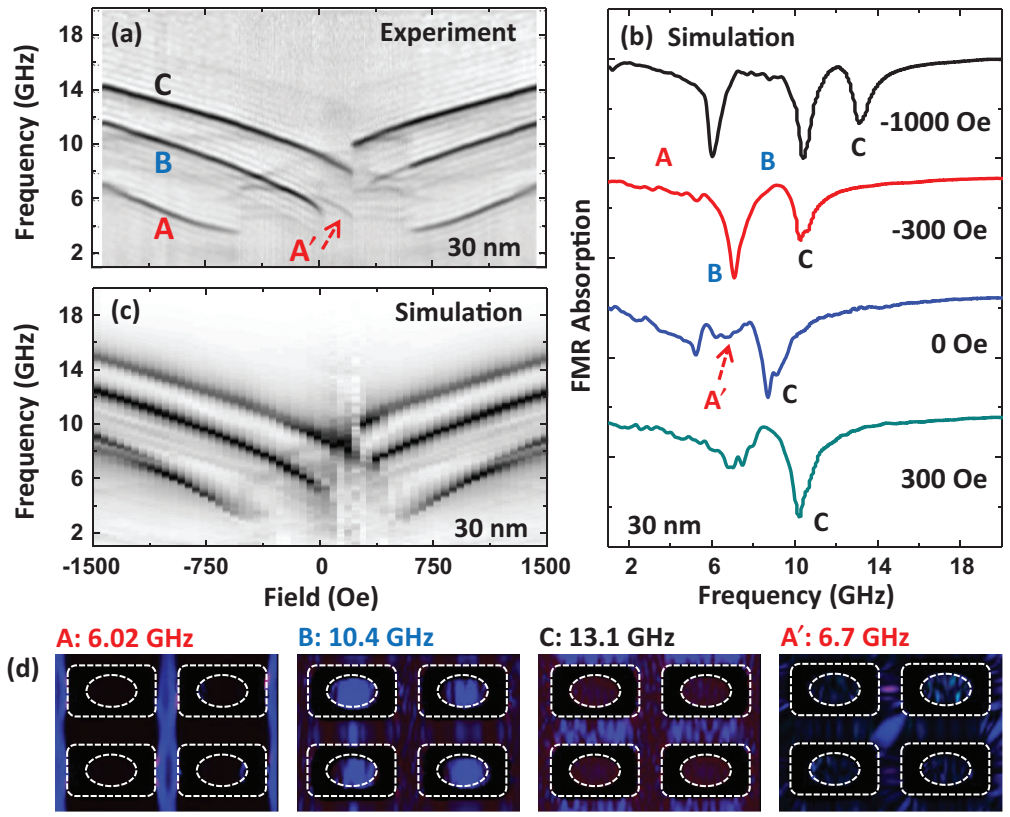

FIG. 3. (Color online) (a) and (c) The experimental and simulated 2D absorption spectra, respectively. (b) Simulated FMR absorption traces of the anti-ring array with varying H_{app} and (d) the spatial distributions of spin precession amplitudes of modes A, A′, B, and C. The distributions for modes A, B, and C are shown for $H_{app} = -1000$ Oe (first three figures) and for mode A′ for H_{app} 0 Oe (the fourth figure).

corresponding to the modes A, B, and C, respectively, which are observed in the simulated absorption curve for $H_{app} = -1000$ Oe. These panels clearly identify the source of each mode. It can be observed that mode A can be approximated by the center mode of a transversely magnetized NW in area A and A′ as previously observed in usual anti-dot arrays, mode B is strongly localized in the central nanomagnet, and mode C originates from the area between two nearest-neighbor cells along the y direction (area C). The FFT image for 6.7 GHz shows that mode A′ for $H_{app} = 0$ Oe originates from area A′. This result agrees with our previous analysis for Fig. 2(d). The simulated 2D FMR spectra [Fig. 3(c)] are also in quantitative accordance with the experimental results [Fig. 3(a)].

IV. THE EFFECT OF THE FILM THICKNESS

As reported in previous work, the dynamic properties of the nanostructure also strongly depend on the thickness of the film t.[31–33] In Sec. IV A, we first investigate the effect of t on the switching process of the nanostructure by performing MOKE and MFM measurements. The dynamic responses of the nanostructures with various film thicknesses will be discussed in Sec. IV B. A series of simulations are shown in Sec. IV C in order to demonstrate that behavior of the anti-dot lattice can be used to detect the magnetic properties of the central nanomagnets.

A. Static behavior

Figure 4(a) shows the measured MOKE loops as a function of the sample thickness. H_{app} was applied in the direction of the x axis for all the structures. A one-step switching process can be observed for the 8-nm-thick anti-ring array. This is in contrast to the multistep switching process for the thicker nanostructures (15, 23, 30, and 40 nm). This difference may be due to the vortex and the multidomain states becoming unstable for the thinnest (i.e., 8-nm-thick) sample. This reduces the difference in the nucleation H_n and annihilation fields for the vortex core inside the central nanomagnets. Switching of the nanomagnets is not observable in the measured M-H loop for the 8-nm-thick sample because the switching field for them overlaps with the switching field of the surrounding anti-dot structure. When the film thickness is increased to 15 nm, the slop of the hysteresis loop changes at around 70 Oe. This evidences formation of a vortex (or a multidomain) state in the central nanomagnets. This state becomes stable when the film thickness is further increased, which is similar to the previously studied case of circular dots.[31] This scenario is supported by the observed decrease in H_n from 70 to −70 Oe when the film thickness is increased from 15 to 40 nm. The switching process for the samples with $t = 15$, 23, 30, and 40 nm is similar to that for the one with $t = 30$ nm, which was discussed in the previous section. Similar to previous reports,[18,33] we also found that the switching field of the surrounding anti-dot lattice increases as the film thickness increases (provided the thickness is much smaller than the characteristic in-plane structure dimension).

In order to verify the analysis given above, we have performed micromagnetic simulations of the magnetization ground state and MFM imaging for the anti-ring arrays with different thicknesses. Figure 4(b) shows the simulated

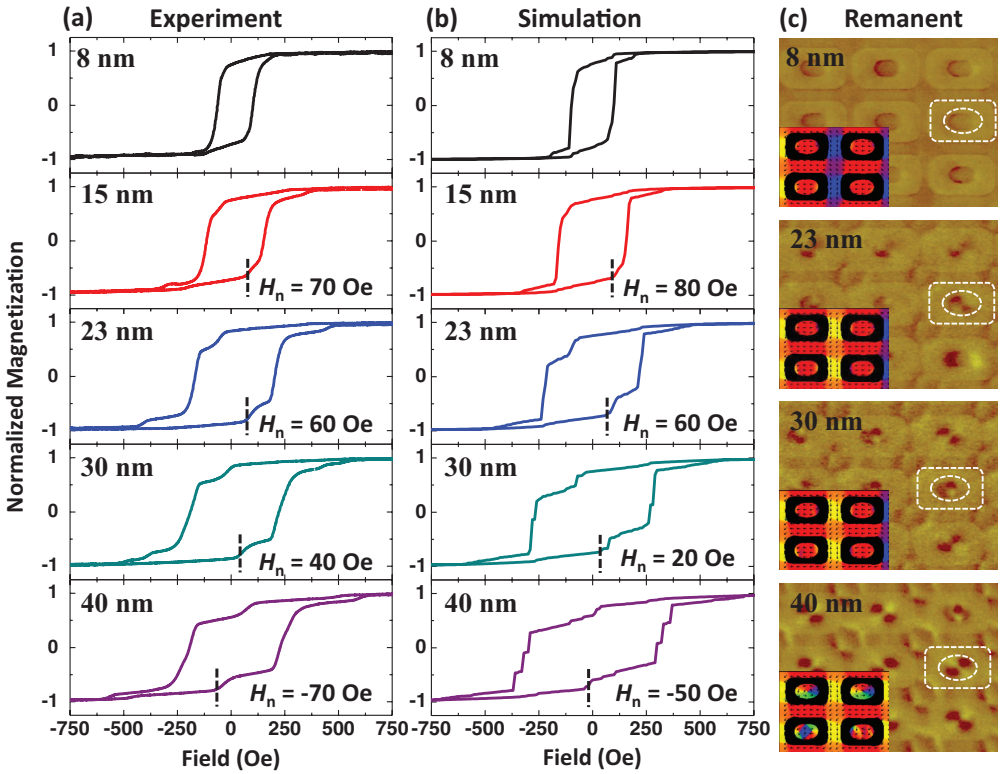

FIG. 4. (Color online) Experimental (a) and simulated (b) M-H loops for the anti-ring arrays with different film thickness. (c) The MFM images of the remanent magnetization state of the anti-ring arrays with differerent film thickness.

hysteresis loops as a function of the film thickness. By comparing with Fig. 4(a), we found that there is a good agreement between the experimental results and the simulated results for all the film thicknesses. The nucleation field H_n for the nanostructure decreases from 80 to −50 Oe when the film thickness is increased from 15 to 40 nm. Similar to the experimental results, the simulated switching field of the surrounding anti-dot array is increased as the film thickness increases. The slight difference between the simulation and the experimental results may be due to a limited number of unit cells and the periodic boundary conditions in both in-plane directions having been used in the simulation. Also, the assumption that the roughness is uniform across the entire sample may have had some influence on the simulation results.

We have further characterized the static magnetic properties using MFM imaging at zero field after first applying a negative saturation field of −1500 Oe as shown in Fig. 4(c). The simulated magnetization states at remanence are shown as the insets to the corresponding MFM images. The simulated remanent magnetization state suggests that the variation in magnetization for $t = 8$ nm at low $|H_{\text{app}}|$ is due to rotation of spins in area A of the nanostructure. The central nanomagnet remains in the saturated state as evidenced by both MFM imaging and simulation [Fig. 4(c)].This agrees with our previous analysis. The results for $t = 15$ nm (not shown in the figure) are identical with that for $t = 8$ nm. One observes some discrepancies between the simulated remanent state and the MFM images for $t = 23$ and 30 nm. The simulation results suggest that the central nanomagnets still remain in the saturated state, while the MFM images show that most of the nanomagnets are in the vortex state or multidomain state. We speculate that it is the MFM measurement process that gives rise to this disagreement. The MFM tip may trigger switching of the central nanomagnets because a nanomagnet prefers to form a vortex or multidomain state for larger sample thicknesses. For the 30-nm-thick sample, all the nanomagnets are in the vortex or multidomain state, while for $t = 23$ nm, some nanomagnets still remain in the saturated state. The MFM image for the 40-nm-thick nanostructure is in qualitative agreement with the simulation of the remanent state. Both MFM imaging and simulation prove that the central nanomagets switch by forming a vortex or multidomain state when the film thickness is increased.

B. Dynamic behavior

The dynamic properties of the nanostructures have also been probed as a function of the film thickness. Shown in Fig. 5(a) are representative FMR absorption curves of the nanostructures with different film thicknesses for $H_{\text{app}} = -1000$ Oe. Three main absorption peaks are clearly identified for all thicknesses. We observed that the frequency of mode A decreases, while those of modes B and C increase with an increase in the sample thickness. The whole nanostructure is in the saturated state for this field as suggested by the hysteresis loops [Fig. 3(a)].

The resonance frequencies of the three modes are summarized in Fig. 5(b) as a function of the film thickness. The micromagnetic simulations of magnetization dynamics have also been performed for different sample thicknesses. These results are also shown in the same figure. There is a good qualitative agreement between the results of simulations and experimental data in terms of the trend of variation of the frequency as a function of the nanostructure thickness.

The dynamic responses of the nanostructures at the remanence also contain important information. Shown in Fig. 5(c) are representative FMR absorption curves for $H_{\text{app}} = 0$ Oe. Similar to the results for the 30-nm-thick sample [Fig. 2(d)], three modes can be observed in all traces except for $t = 40$ nm, which is the largest thickness. For the 40-nm-thick nanostructure mode B is not visible. This phenomenon represents more evidence that the central nanomagnet is in a vortex or multidomain state for $t = 40$ nm, as we discussed above (Fig. 4). We have also simulated the amplitudes of the dynamic response of the nanostructure for $H_{\text{app}} = 0$ Oe to identify the origin of each mode. The FFT images of the dynamic magnetization for the 10-nm-thick nanostructure and for particular frequencies 3.2 GHz (mode B) and 4.1 GHz (mode A′) are shown in Fig. 5(d). The left-hand image demonstrates that the large spin precession amplitude in area B is the origin of mode B. The right-hand one clearly shows that mode A′ is localized in area A′ as we discussed in Fig. 3(d). The spatial distribution of spin precession amplitudes for mode C is similar to the result shown in Fig. 3(d) and, therefore, is not shown.

The peak shifts for modes B and C as functions of t can also be observed for $H_{\text{app}} = 0$ Oe. The Kittel's equation[29] is still qualitatively applicable for these two modes because the areas of localization for these two modes remain in the saturated state at the remanence. One also notices that the intensity of mode B is noticeably lower than that of mode C for 30 nm, which is in great contrast to the thinner nanostructures. The unstable saturated state of the central nanomagnets may be the main cause of this effect.

The difference in dynamic responses between the thick and thin anti-ring arrays becomes obvious while comparing the experimental 2D absorption spectra for the 8-nm and 40-nm-thick samples [Figs. 5(e) and 5(f), respectively]. The three modes are unambiguously identified in the field range from −1500 to −200 Oe, while the modes A and B for $t = 40$ nm vanish when $H_{\text{app}} = -600$ and −70 Oe, respectively. The disappearance of the two modes agrees with the rotation of the spin direction in area A (mode A) and the switching to the vortex state of area B (mode B) as shown in the hysteresis loop.

C. Effect of the presence of the nanomagnets inside the anti-dot holes

In order to better understand the effect of the central nanomagnet inside the anti-dot array, we have performed the simulations of magnetic properties of the anti-dot array and of the central nanomagnet separately as functions of the film thickness. Shown in Figs. 6(a)–6(c) are the simulated magnetization states for the 30-nm-thick anti-ring array, the respective anti-dot array, and the array of nanomagnets with the same shape as the central dot. These diagrams correspond to $H_{\text{app}} = -1000$ Oe. The nanostructures are almost magnetically saturated for this field value. The vector of magnetization in the area near the edges of the nanostructure is slightly tilted due to shape anisotropy. α (α', α''), β (β', β''), and γ (γ',

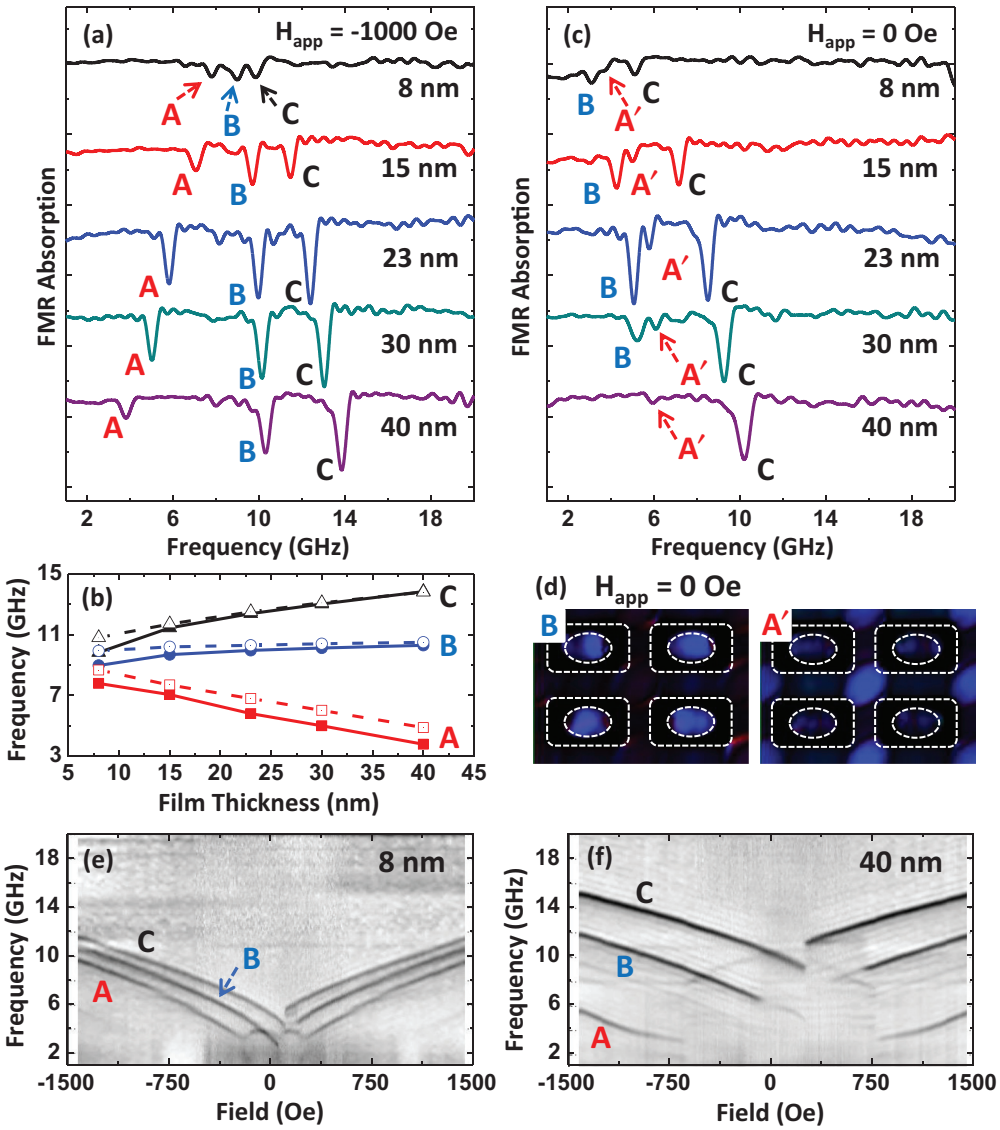

FIG. 5. (Color online) FMR spectra for anti-ring arrays with $t = 8$, 15, 23, 30, and 40 nm at $H_{app} = -1000$ Oe (a) and 0 Oe (c). (b) The extracted experimental (solid symbols) and simulated (open symbols) resonance frequencies for different modes as a function of thickness. (d) The spatial distribution of spin precession amplitudes for modes B and A″. The experimental 2D absorption spectra of anti-ring arrays with $t = 8$ and 40 nm are shown in (e) and (f), respectively.

γ'') are the centers of areas C, A′ and A for the anti-ring array (anti-dot array and central nanomagnet array). The x components of the demagnetizing fields of the anti-ring and the anti-dot arrays have been extracted and summarized as functions of the film thickness in Fig. 6(d). We found that the demagnetizing field of the anti-ring array (solid symbols) for point α is very weak and does not vary significantly as the film thickness is increased. We also found that the demagnetizing effect clearly increases as the film thickness is increased for points β and γ.

Interestingly, the demagnetizing field of the nanostructure is weaker for points β and γ, and it is larger for point α than for the anti-dot array because of the stray field of the central nanomagnets. This field is anti-parallel to the demagnetizing field of the edge of the anti-dot structure at the point α. This can be checked by extracting the stray field of the central nanomagnets at the same position [Fig. 6(e)]. It clearly shows that the direction of the stray field of the dot at position α is anti-parallel to that for positions β and γ. In the same figure, we also plotted the difference in the demagnetizing fields between the anti-ring array and the anti-dot array α–α', β–β', and γ–γ' (open symbols). These plots show the same trend. The mismatch for position β and γ for larger thicknesses may be due to the tilted spin direction around the edges of the nanostructures. These results suggest that anti-ring structures may have potential for applications in detectors magnetic micro- or nanoparticles, similar to the bioanalytical measurement tools shown in Ref. 22. Indeed, the presence of magnetic material inside the holes noticeably modifies the FMR response of the host anti-dots. Basically, in order to detect the presence of a small-sized object, one needs a probing object of similar dimensions. Otherwise, the contribution to the energy of the probing object due to the interaction with the detected object will be negligible. The holes of the nanodot

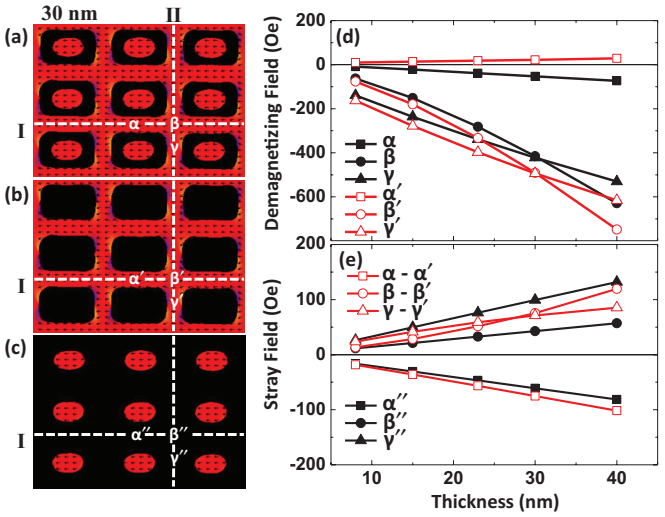

FIG. 6. (Color online) Simulated magnetization state of the (a) anti-ring, (b) anti-rectangle, and (c) ellipse for 30-nm film thickness when $H_{app} = -1000$ Oe. (d) The internal field value in different areas of anti-ring and anti-rectangle structure as a function of the film thickness for $H_{app} = -1000$ Oe. (e) The stray field in different areas of the ellipse array as a function of the film thickness for $H_{app} = -1000$ Oe.

structures may serve as such probing objects for magnetic nanoparticles as our study suggests.

This leads to the potential application of the anti-ring arrays in antigen detectors. We suggest a concept as follows. Following Ref. 34, magnetic nanoparticles can be biofunctionalized such that they bind to a specific antigen and thus function as tags for the antigen. The central dots are biofunctionalized in a similar way. The target antigen is captured by a nanoparticle from solution. As the magnetic nanoparticle diffuses to the central dot, the captured antigen also binds to the detection antibody attached to the dot and becomes sandwiched between the two antibodies and immobilized. The presence at the surface of the central dot of a magnetic nanoparticle captured in this way shifts the frequency of the dot's FMR mode. The amplitude of the extra FMR absorption peak emerging at the shifted frequency will scale as a number of nanoparticles attached to the central dots.

V. CONCLUSION

We have carried out a systematic experimental investigation of the static and dynamic responses of the anti-ring arrays as a function of the film thickness using broadband FMR spectroscopy, MOKE, and MFM. The multiple absorption peaks observed for the anti-ring structures are attributed to the superposition of the absorptions by the anti-dot lattice and the central nanomagnets. The static and dynamic behaviors are markedly sensitive to the film thickness due to the complex demagnetizing field distributions as validated by direct MFM imaging. Our results are in agreement with micromagnetic simulations of static and dynamic properties of the nanostructures.

ACKNOWLEDGMENTS

This work was supported by SMF-NUS New Horizon Awards, Ministry of Education, Singapore, and the Australian Research Council.

*Corresponding author: eleaao@nus.edu.sg

[1] A. O. Adeyeye and N. Singh, J. Phys. D **41**, 153001 (2008).
[2] S. Neusser and D. Grundler, Adv. Mater. **21**, 2927 (2009).
[3] S. A. Nikitov, P. Tailhades, and C. S. Tsai, J. Magn. Magn. Mater. **236**, 320 (2001).
[4] K. S. Lee and S. K. Kim, J. Appl. Phys. **104**, 053909 (2008).
[5] S. Choi, K.-S. Lee, K. Y. Guslienko, and S.-K. Kim, Phys. Rev. Lett. **98**, 087205 (2007).
[6] A. Khitun, M. Bao, and K. L. Wang, J. Phys. D **43**, 264005 (2010).
[7] J. Topp, D. Heitmann, M. P. Kostylev, and D. Grundler, Phys. Rev. Lett. **104**, 207205 (2010).
[8] J. Ding, M. Kostylev, and A. O. Adeyeye, Phys. Rev. Lett. **107**, 047205 (2011).
[9] J. Topp, S. Mendach, D. Heitmann, M. Kostylev, and D. Grundler, Phys. Rev. B **84**, 214413 (2011).
[10] S. Neusser, G. Duerr, H. G. Bauer, S. Tacchi, M. Madami, G. Woltersdorf, G. Gubbiotti, C. H. Back, and D. Grundler, Phys. Rev. Lett. **105**, 067208 (2010).
[11] A. V. Chumak, A. A. Serga, B. Hillebrands, and M. P. Kostylev, Appl. Phys. Lett. **93**, 022508 (2008).
[12] Z. K. Wang, V. L. Zhang, H. S. Lim, S. C. Ng, M. H. Kuok, S. Jain, and A. O. Adeyeye, Appl. Phys. Lett. **94**, 083112 (2009).
[13] G. Gubbiotti, S. Tacchi, G. Carlotti, P. Vavassori, N. Singh, S. Goolaup, A. O. Adeyeye, A. Stashkevich, and M. Kostylev, Phys. Rev. B **72**, 224413 (2005).
[14] C. C. Wang, A. O. Adeyeye, and N. Singh, Nanotechnology **17**, 1629 (2006).
[15] D. H. Y. Tse, S. J. Steinmuller, T. Trypiniotis, D. Anderson, G. A. C. Jones, J. A. C. Bland, and C. H. W. Barnes, Phys. Rev. B **79**, 054426 (2009).
[16] C. Yu, M. J. Pechan, and G. J. Mankey, Appl. Phys. Lett. **83**, 3948 (2003).
[17] M. H. Yu, L. Malkinski, L. Spinu, W. L. Zhou, and S. Whittenburg, J. Appl. Phys. **101**, 3 (2007).
[18] O. N. Martyanov, V. F. Yudanov, R. N. Lee, S. A. Nepijko, H. J. Elmers, R. Hertel, C. M. Schneider, and G. Schonhense, Phys. Rev. B **75**, 174429 (2007).
[19] J. Ding, D. Tripathy, and A. O. Adeyeye, Europhys. Lett. **98**, 16004 (2012).
[20] G. Duerr, M. Madami, S. Neusser, S. Tacchi, G. Gubbiotti, G. Carlotti, and D. Grundler, Appl. Phys. Lett. **99**, 202502 (2011).
[21] X. M. Liu, J. Ding, and A. O. Adeyeye, Appl. Phys. Lett. **100**, 242411 (2012).
[22] A. L. Washburn and R. C. Bailey, Analyst **136**, 227 (2011).

[23]N. Singh, S. Goolaup, and A. O. Adeyeye, Nanotechnology **15**, 1539 (2004).
[24]H. Chen, P. De Gasperis, and R. Marcelli, IEEE Trans. Magn. **29**, 3013 (1993).
[25]M. R. Scheinfein, LLG Micromagnetics Simulator, software for micromagnetic simulations, http://llgmicro.home.mindspring.com (last accessed June 2013).
[26]J. P. Park, P. Eames, D. M. Engebretson, J. Berezovsky, and P. A. Crowell, Phys. Rev. Lett. **89**, 277201 (2002).
[27]M. Buess, R. Hollinger, T. Haug, K. Perzlmaier, U. Krey, D. Pescia, M. R. Scheinfein, D. Weiss, and C. H. Back, Phys. Rev. Lett. **93**, 077207 (2004).
[28]R. D. McMichael, and M. D. Stiles, J. Appl. Phys. **97**, 10J901 (2005).
[29]C. Kittel, Phys. Rev. **73**, 155 (1948).
[30]F. G. Aliev, J. F. Sierra, A. A. Awad, G. N. Kakazei, D. S. Han, S. K. Kim, V. Metlushko, B. Ilic, and K. Y. Guslienko, Phys. Rev. B **79**, 174433 (2009).
[31]R. P. Cowburn, D. K. Koltsov, A. O. Adeyeye, M. E. Welland, and D. M. Tricker, Phys. Rev. Lett. **83**, 1042 (1999).
[32]J. M. Shaw, T. J. Silva, M. L. Schneider, and R. D. McMichael, Phys. Rev. B **79**, 184404 (2009).
[33]K. Liu and C. L. Chien, IEEE Trans. Magn. **34**, 1021 (1998).
[34]R. S. Gaster, D. A. Hall, C. H. Nielsen, S. J. Osterfeld, H. Yu, K. E. Mach, R. J. Wilson, B. Murmann, J. C. Liao, S. S. Gambhir, and S. X. Wang, Nat. Med. **15**, 1327 (2009).